Luminescent two-color tracer particles for simultaneous velocity and temperature measurements in microfluidics

OPEN ACCESS
IOP Publishing
Measurement Science and Technology
Meas. Sci. Technol. **27** (2016) 115301 (12pp)
doi:10.1088/0957-0233/27/11/115301

Luminescent two-color tracer particles for simultaneous velocity and temperature measurements in microfluidics

J Massing[1], D Kaden[2], C J Kähler[1] and C Cierpka[1]

[1] Institute for Fluid Mechanics and Aerodynamics, Bundeswehr University Munich, 85577 Neubiberg, Germany
[2] Surflay Nanotec GmbH, Max-Planck-Str. 3, 12489 Berlin, Germany

E-mail: julian.massing@unibw.de and d.kaden@surflay.com

Received 10 June 2016, revised 10 August 2016
Accepted for publication 22 August 2016
Published 22 September 2016

Abstract

The simultaneous and non-intrusive measurement of temperature and velocity fields in flows is of great scientific and technological interest. To sample the velocity and temperature, tracer particle based approaches have been developed, where the velocity is measured using PIV or PTV and the temperature is obtained from the intensity (LIF, thermographic phosphors) or frequency (TLC) of the light emitted or reflected by the tracer particles. In this article, a measurement technique is introduced, that relates the luminescent intensity ratio of individual dual-color luminescent tracer particles to temperature. Different processing algorithms are tested on synthetic particle images and compared with respect to their accuracy in estimating the intensity ratio. Furthermore, polymer particles which are doped with the temperature sensitive dye europium (III) thenoyltrifluoroacetonate (EuTTA) and the nearly temperature insensitive reference dye perylene are characterized as valid tracers. The results show a reduction of the temperature measurement uncertainty of almost 40% (95% confidence interval) compared to previously reported luminescent particle based measurement techniques for microfluidics.

Keywords: particle tracking thermometry/velocimetry, temperature sensitive particles, laser induced fluorescence, microfluidics

(Some figures may appear in colour only in the online journal)

1. Introduction

Convective heat transfer is a common physical process often encountered in fluidmechanics, especially in microfluidics (Yoshida 2005). It is governed by a complex interaction between a fully three-dimensional velocity field and the superimposed temperature field. A better understanding of this phenomenon is a key factor for future developments in various engineering disciplines, such as process engineering, transportation, communication and many more. For instance, great advances in the miniaturization of electronic components have been made during the last decade, partly due to more efficient heat management systems. Heat transfer plays also a major role in chemical engineering. The yield of a chemical reaction can be increased by controlling the temperature at the most desirable point. This could lead to a better performance of microfluidic fuel-cells (Faghri and Guo 2005). Therefore, a technique for simultaneous non-intrusive measurements of the velocity and the temperature field is necessary.

Particle image velocimetry (PIV) and particle tracking velocimetry (PTV) are well established optical methods for the non-intrusive measurement of velocity fields (Kähler *et al* 2016). The fluid is seeded with particles that should faithfully

follow the flow. The region of interest is illuminated with a laser light sheet or via volume illumination and a series of consecutive images or image pairs is taken at a known time difference. The velocity field can then be estimated by the particles' displacement and the elapsed time between two images after a proper calibration. For PIV the images are subdivided into small interrogation windows which are cross-correlated. The displacement of a particle image ensemble at each location is proportional to the shift of the correlation peak in the respective interrogation window. In PTV the velocity vector can be computed for each particle image individually even for comparatively high seeding concentrations (Cierpka *et al* 2013). Thus, in contrast to PIV this technique does not show a bias error, when strong velocity gradients are present in the flow (Kähler *et al* 2012). Therefore, PTV is better suited in the case of large in-plane as well as out-of-plane gradients (Kähler *et al* 2012), as typical in microfluidics. This makes the technique ideally suited for the evaluation of microfluidic systems (Cierpka and Kähler 2012).

A common optical method for measuring the temperature field with high resolution in macroscopic flows (Sakakibara and Adrian 1999, Shafii *et al* 2010), as well as in microscopic flows (Natrajan and Christensen 2009, Kim and Yoda 2010) is laser induced fluorescence (LIF). The technique relies on dissolving fluorescent dyes in the fluid, that exhibit a fluorescent intensity which is highly dependent on the surrounding temperature (Crimaldi 2008). To account for spatial or temporal variations in the excitation energy, a two-color approach is often applied, where two fluorescent dyes with different temperature dependencies and different emission spectra are dissolved in the fluid under investigation and the temperature is estimated from the ratio of the two fluorescent signals. However, LIF has similar drawbacks as PIV does when it is applied to microfluidics. Due to the volume illumination, dye molecules outside of the in-focus plane significantly contribute to the fluorescent signal. This introduces a bias error, when out-of-plane temperature gradients are present. Consequently, temperature sensitive tracer particles have to be used to simultaneously measure the temperature and velocity field, without bias errors.

One type of luminescent particles that have often been used for this task are so called thermographic phosphors (Aldén *et al* 2011). They are temperature sensitive over a large temperature range and at high temperatures (300 K–2000 K) and show an intensity change in the order of 0.3% K^{-1} (Fond *et al* 2012, 2015)). This limits their applicability to microfluidic flows, where in most cases smaller temperature variations are present. Furthermore, currently available particles are randomly shaped and not spherical, which reduces the precision in estimating the particle center position through PTV for large optical magnifications. Additionally, it is relatively difficult to uniformly suspend phosphor particles in water. Therefore, even phosphors with a higher temperature sensitivity, such as ZnO phosphors ($\sim$1% K^{-1}, Abram *et al* (2015)), are presently not used in microfluidic experiments.

Vogt and Stephan (2012) measured the temperature and velocity field in a flow driven by natural convection as well as in a pressure driven flow inside a capillary tube using fluorescent tracer particles. To estimate the temperature and the velocity field the camera images were divided into smaller interrogation windows and the temperature and velocity values for each window were calculated. For the temperature estimation, this resulted in an uncertainty of $\pm$3.4 K for a 95% confidence interval in the case of natural convection, when temporal averaging over 20 images was used. For the microfluidic experiment with the capillary tube, a measurement uncertainty of $\pm$8.6 K and $\pm$6.9 K (95% confidence interval) was obtained with temporal averaging over 500 images, depending on the flow rate and thus on the number of particle images captured during one experiment. However, since the authors did not use particle tracking, only averaged values for the interrogation windows could be obtained, which limited the spatial resolution.

Another option for temperature sensitive particles is the use of so called thermochromic liquid crystals (TLCs), which reflect different parts of the visible spectrum of light depending on their temperature. Thus, when the particles are illuminated by white light and imaged on a color-camera, the color of the particle images can be related to the temperature in the fluid. This technique is known as particle image thermometry (PIT) and has been introduced nearly 30 years ago for simultaneous velocity and temperature field measurements by combining PIV and PIT (Kimura *et al* 1988, Hiller *et al* 1993). Recently, Schiepel *et al* (2016) combined PIT with tomographic PIV to simultaneously measure the volumetric velocity and temperature field in turbulent Rayleigh–Bénard convection. A comprehensive review of the technique can be found in Dabiri (2009). Under ideal conditions, uncertainties in the temperature estimation lower than 0.1 K were reported for particle ensembles depending on the width of the working temperature band of the TLCs, which can range from 0.5 K to 20 K for currently available TLC materials (Kim *et al* 2015). Segura *et al* (2013) adapted the measurement method for microfluidic applications, by evaluating individual non-encapsulated TLCs. The authors reported a measurement uncertainty of 4.9% over 13 K with a 95% confidence interval. Segura *et al* (2015) used this technique to simultaneously measure the volumetric (3D3C) velocity- and temperature field in an evaporating droplet with high resolution. However, long exposure times were necessary. Therefore, the technique it was only applicable to slow flows (Segura 2014).

To overcome the aforementioned limitations, the aim of this article is to provide a reliable method for evaluating the luminescent intensity signals of individual particle images to measure temperature fields. Different means of calculating the intensity ratio of individual particle images will be investigated and compared with the help of synthetic particle images. Furthermore, luminescent polymer micro particles doped with the temperature sensitive dye europium (III) thenoyltrifluoroacetonate (EuTTA) and the nearly temperature insensitive dye perylene will be characterized as valid tracer particles for simultaneous velocity and temperature field measurements.

2. Sampling and processing of individual particle images

The investigation presented in this article is based on the assumption that particle images can be approximated by a

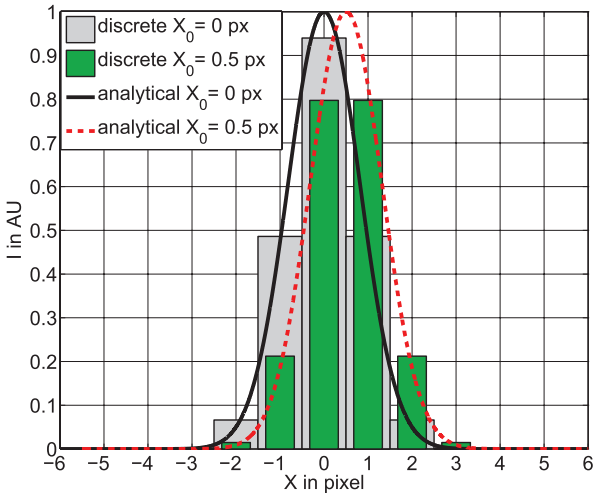

Figure 1. The analytical intensity distribution for a particle image with a diameter of $D_p = 3$ pixel at $X_0 = 0$ pixel and $X_0 = 0.5$ pixel and the corresponding signals on discrete pixels without noise.

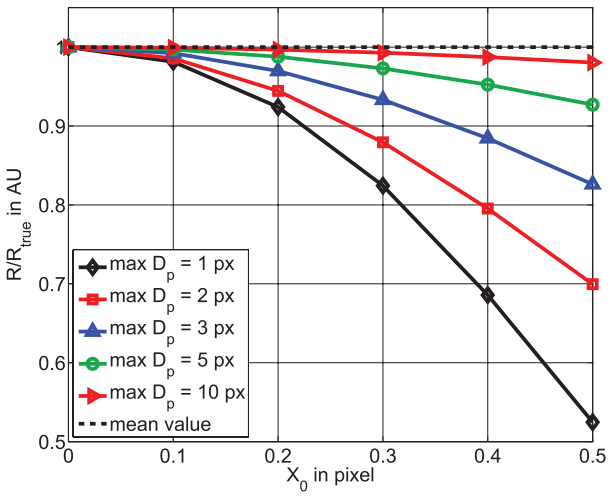

Figure 2. Ratio of the maximum intensities for particle images with different diameters D_p at changing sub-pixel positions.

two-dimensional circular symmetrical Gaussian function. This simplification is valid for diffraction limited imaging, which holds for the imaging of particles with a diameter of less than 10 μm (Adrian 1991) as well as for infinity corrected optics, which are commonly installed in the microscopes used in microfluidics (Meinhart and Wereley 2003). However, the analytical intensity distribution of a particle image is sampled on the discrete pixels of a camera sensor. Therefore, the actual intensity value of each pixel is an integrated value of the Gaussian. Figure 1 shows in one dimension the analytical and discrete intensity distribution of a particle image with a diameter of $D_p = 3$ pixel[3] located at a center position of $X_0 = 0$ pixel and $X_0 = 0.5$ pixel, i. e. at the interface between two pixels. It can clearly be seen that although the analytical intensity distributions are equal, there is a difference of almost 20% between the maximum intensity values of the discrete particle images, due to the shift in the sub-pixel position even without any additional noise. As the set up for the ratiometric measurement method consists of two independent cameras or sensors, which image the same area of view, it will hardly be possible to match both cameras on the sub-pixel level. Therefore, it is likely that the appearance of the same particle on each camera image differs according to figure 1. Consequently, the sub-pixel shift of the particle images between the two cameras can cause large bias errors, if the intensity maximum is used for rationing. The size of this bias error increases with decreasing particle image diameter and increasing difference in sub-pixel position as can be seen in figure 2. For a particle with a diameter of $D_p = 1$ pixel, the calculated ratio is only 52% of the true ratio ($R/R_{true} = 0.52$) at the maximum sub-pixel offset of $X_0 = 0.5$ pixel. As small particle image diameters are also disadvantageous for velocity measurements due to the peak locking effect the following analysis assumes particle images of 3 or more pixel extension, as typical in microfluidic applications. Nonetheless, the ratio between the calculated and the true intensity ratio $R/R_{true} = 0.83$ at the maximum sub-pixel offset is still too far away from unity, to yield reliable measurement results. Fortunately, the bias error due to the different sub-pixel positions in both camera images can be assessed prior to the experiments for different combinations of particle image diameter and sub-pixel position. Since modern particle tracking algorithms are able to estimate the particle image position and diameter within subpixel accuracy (Cierpka *et al* 2010), the measurements can be corrected for the sub-pixel error.

Alternatively to the peak intensity values it is also possible to use the mean intensity of the particle image for rationing. Figure 2 shows that the mean value is not affected by the sub-pixel shift between the camera images, as expected, because the same intensity is just distributed over a different number of pixels, so that the integral or mean intensity values are identical. To detect particle images and their diameter, usually a constant threshold is defined to segment the camera image. A conjugated group of pixels that lie above that threshold and comply with other specified criteria (e.g. minimal/maximal diameter) will be regarded as a particle image. However, when two fluorescent dyes are used, the intensity of the reference dye stays approximately constant throughout the experiment, whereas the intensity of the dye that is sensitive to the measured scalar will change depending on the value of the quantity. Consequently, the intensity distribution of one of the particle images will be lower than the other one, depending on the value of the scalar. In figure 3 the analytical distribution of two particle images with an intensity ratio of $I_{max,2}/I_{max,1} = 0.7$ and a particle image diameter of $D_p = 3$ pixel is shown. The green area depicts the part of the intensity distribution of the darker signal that will be regarded as a particle image, if a global segmentation value of 0.1 is used. It can be seen, that the detected diameter of the darker signal, is smaller than the diameter of the brighter particle image. Therefore, the mean intensity of the lower signal will be estimated as too high, which will lead to a bias error in the intensity ratio of both signals. To obtain the correct ratio, the detected diameters of associated particle images have to be equal. In principle, this can be achieved by adapting the segmentation value for each particle image

[3] A fill factor of one is assumed here (all the light on the surface is integrated on the corresponding pixel).

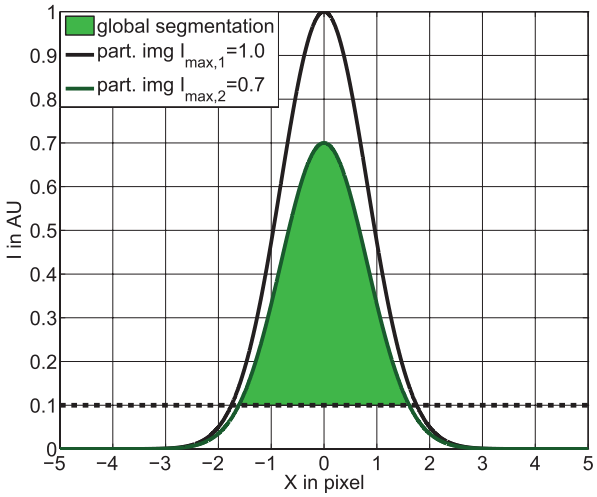

Figure 3. Analytical intensity distribution of two particle images with an intensity ratio of $I_{max,2}/I_{max,1} = 0.7$ and a diameter of $D_p = 3$ pixel and the area that will be considered as the darker particle image in processing for a global segmentation threshold of 0.1.

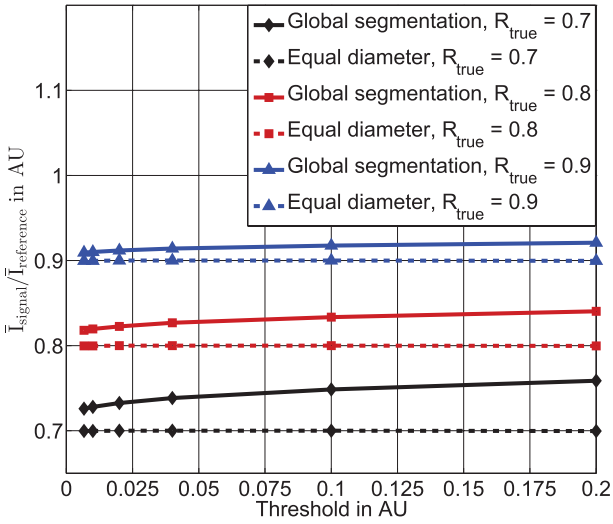

Figure 4. Calculated intensity ratio for globally segmented particle images and particle images with equal diameters ($D_p = 3$ pixel) for varying true intensity ratios and segmentation threshold.

individually, but this is very difficult to realize. A more convenient method is to detect the particle images for both cameras using a global threshold value and then prescribing one of the detected diameters for both particle images. In figure 4 the calculated intensity ratio for different segmentation thresholds and true intensity ratios for both methods (global segmentation and equal diameter, $D_p = 3$ pixel) are shown. It can clearly be seen, that the size of the bias error increases with increasing segmentation threshold and decreasing intensity ratio. It can be fully avoided by setting the particle image diameters to the same value.

In the case of ideal images, using the corrected maximum intensity or the mean intensity value with equal diameters yields equally accurate results for the intensity ratio. However, in reality the obtained images are subjected to noise, which adds as a random error. It can be assumed that noise influences the results of both processing methods differently. Therefore, synthetic images with different signal to noise ratios ($SNR = \overline{I_{max}}/2\sigma$, where σ is the standard deviation of the camera noise and $\overline{I_{max}}$ is the average of the maximum signal intensities of all particle images) and particle image diameters were created and used for the test of both methods.

3. Synthetic particle images

Analyzing synthetic images is a common method to test and validate processing algorithms (Kähler *et al* 2012, Kähler *et al* 2016). The investigated parameters can be fully controlled, as opposed to an experiment, where additional uncertainties exist, such as the imaging optics, particle properties, illumination power and pulse-to-pulse stability and many more. Furthermore, single parameters can be changed individually and the parameter range can be extended beyond what is experimentally accessible. For the following analysis the real camera image of a 16 bit sCMOS camera was simulated by randomly distributing 150 synthetic particle images with a Gaussian intensity distribution over an area of 2160×2560 pixel. This corresponds to a relatively low seeding concentration, which was chosen to avoid particle image overlapping. To reproduce the effects arising from the sampling of the analytical intensity distribution on the discrete pixels of a camera chip, the gray value of each pixel was calculated by integrating the intensity over the corresponding pixel area. This implies the assumption of a camera sensor with a fill factor of one and a constant transfer function. In reality this may not be the case because of micro lenses and the design of the sensor, which causes bias errors as discussed in Kähler (2004). However, this simplification can be neglected for the investiagtion of the sensitivity of the algorithms as aimed by the current study. To investigate the influence of the signal to noise ratio, normal distributed noise with a standard deviation of $\sigma = \overline{I_{max}}/(2 \cdot SNR)$ was added to the synthetic images. To avoid saturation on the 16 bit images, the maximum intensity of the particle images was set to $I_{max} = 0.9 \cdot 2^{16}$.

In the investigated measurement method, the scalar field is estimated by the intensity ratio between a signal and a reference image. Therefore, pairs of synthetic camera images were created, with a constant intensity ratio of $I_{temp}/I_{ref} = 0.9$ between corresponding particle images. However, the absolute noise level was maintained equal for both camera images, which is coherent with experimentally acquired images. A uniformly distributed sub-pixel shift ranging from -0.5 to 0.5 pixels in X and Y direction was introduced between the particle image pairs to investigate the effects arising from the sub-pixel error. Additionally, multiple sets of synthetic particle images were created, with varying particle image diameters ($D_p = 3$–20 pixel) as well as different signal to noise ratios. Thus, the dependency of the processing methods on the characteristic appearance of the particle images can be studied. To reach statistical convergence in the intensity ratio and the standard deviation of the ratio, 7500 independent particle image pairs were evaluated for each combination of particle image diameter and SNR. The particle images in the signal and reference image are identified, by setting a global segmentation threshold of I_{max}/SNR. A 2D Gaussian fit is used to estimate the center and diameter of each

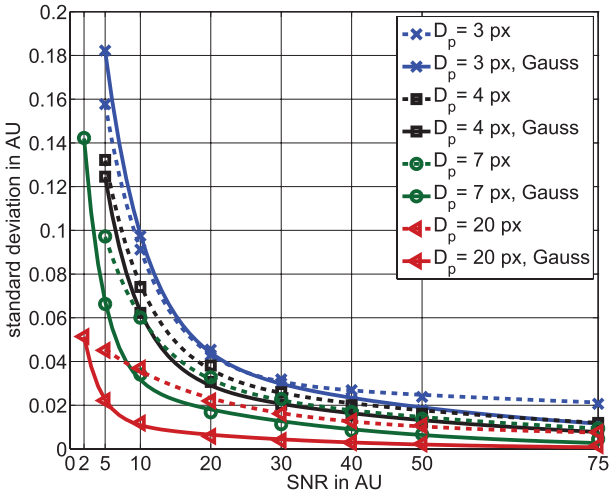

Figure 5. Comparison of the standard deviation of the ratio of the corrected maximum intensity values and the standard deviation of the ratio of the maximum intensity values from the Gaussian fit for different particle image diameters and SNRs.

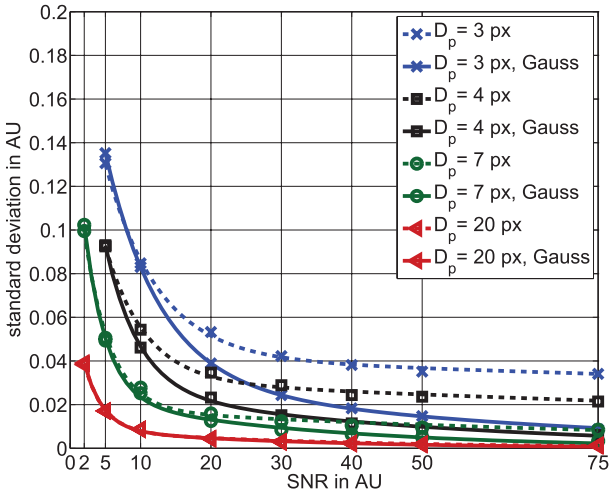

Figure 6. Comparison of the standard deviation of the ratio of the mean raw intensity values and the standard deviation of the ratio of the mean intensity values from the Gaussian fit for different particle image diameters and SNRs.

particle image within sub-pixel accuracy (Kähler *et al* 2012) and the respective intensity ratios were obtained by dividing the peak intensity values, as well as the mean intensity values of corresponding particle images. Because the sub-pixel position of the particle image centers is also estimated by the particle image detection algorithm, the peak intensity ratio can be corrected for the sub-pixel error. To determine the mean intensity ratio, first the particle images' diameter in the signal image was set equal to the corresponding diameters found in the reference image. Then, the arithmetic mean of the intensity values of all pixels within each particle image's diameter was computed and finally the ratio was calculated. No preprocessing or smoothing of the synthetic camera images was done prior to the particle image detection and the calculation of the intensity ratios. However, to reduce the standard deviation in the determination of the intensity ratios with both methods, the noisy intensity distributions of the particle images were approximated by a 2D Gaussian with the least square fitting method.

In order to determine the method which gives the most accurate prediction of the temperature field, the different approaches are compared with regard to the standard deviation, which gives the random error, and the deviation of the estimated intensity ratio from the true intensity ratio. In figure 5 the standard deviation over all particle image ratios that were calculated with the corrected maximum particle image intensity is compared to the standard deviation that was achieved, when the maximum intensity of the Gaussian fit was used for rationing. For better readability only a representative selection of particle image diameters is presented. The results show, that using the maximum of the Gaussian fit to calculate the intensity ratio yields smaller standard deviations, i.e. a better measurement accuracy, than using the corrected maximum intensity, except for a particle image diameter of $D_p = 3$ pixel at SNRs < 20. For the ratios of the corrected maximum, no results are shown for SNR < 5, since the algorithm could not give reliable results for such high noise levels. However, applying the Gaussian fit before calculating

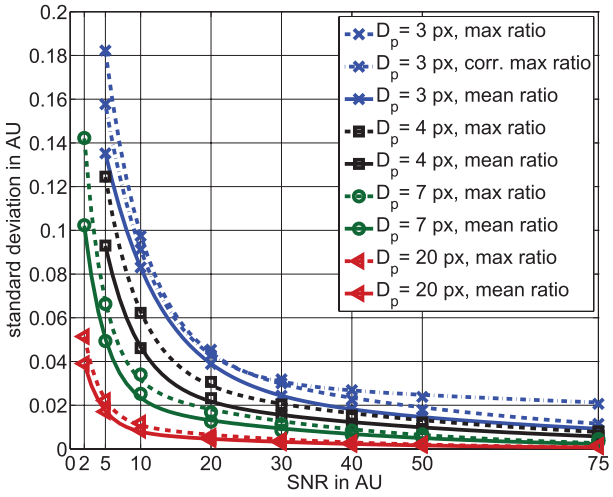

Figure 7. Comparison of the standard deviation of the ratio of the maximum intensity values and the standard deviation of the ratio of the mean intensity values from the Gaussian fit for different particle image diameters and SNRs.

the ratio gave reliable results for SNR $\geqslant 2$ for particle image diameters of $D_p \geqslant 7$. In figure 6 the same comparison is done for the ratios of the mean particle image intensity with equal diameter and the ratios of the mean of the Gaussian fit. Here, the intensity ratio from the Gaussian yields a smaller standard deviation for all investigated particle image diameters and signal to noise ratios. Reliable results for a SNR < 5 could be obtained with both methods only for particle image diameters of $D_p \geqslant 7$ pixel. In figure 7 the rationing methods that yielded the smallest standard deviation for the ratio of the maxima (for $D_p = 3$ pixel and SNR < 20 corrected maximum, else Gaussian fit) and the ratio of the mean intensities (Gaussian fit) are compared. It can clearly be seen, that using the mean of the Gaussian for rationing always leads to a smaller standard deviation. Furthermore, the standard deviation can be approximated as a second order exponential function of the signal to noise ratio. This means that a small improvement of the

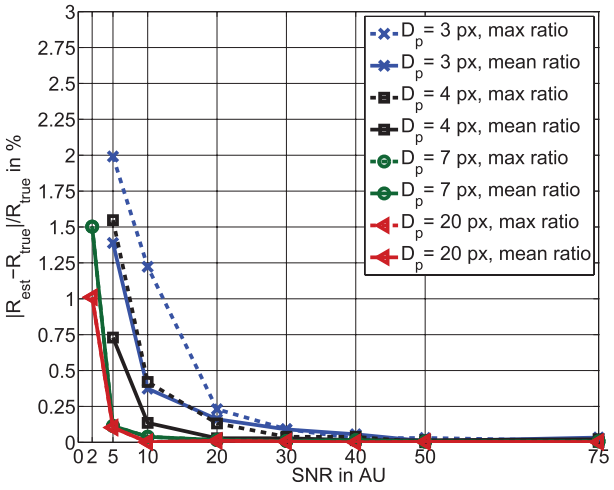

Figure 8. Deviation of the estimated intensity ratio from the true intensity ratio for the methods using the maximum intensity of the Gaussian and the mean intensity of the Gaussian for rationing.

SNR leads to a substantial reduction in the standard deviation for SNRs < 10, thus, largely improving the measurement accuracy. Therefore, a high luminescent signal is an important condition for a reliable temperature estimation.

From the presented results it can be concluded, that approximating the noisy intensity distributions of the particle images with a 2D Gaussian and using the mean value of this fit for rationing, leads to the most accurate results for the intensity ratio of all investigated methods. This finding is supported by figure 8, which shows the deviation of the estimated mean intensity ratio from the true intensity ratio when the maximum of the Gaussian fit and when the mean of the Gaussian fit is used for rationing. For both methods the deviation is smaller than 2 percent of the true ratio and the method calculating the intensity ratio from the mean of the Gaussian shows a smaller deviation. For particle image diameters of $D_p \geqslant 7$ pixel and signal to noise ratios of SNR $\geqslant 5$ the deviation of the estimated intensity ratio from the true intensity ratio is below 0.1%.

4. Characterization of EuTTA/perylene tracer particles

A key factor in achieving reliable particle based temperature field measurements are the tracer particles themselves. They have to possess a variety of very demanding properties to allow for an accurate temperature estimation. First a combination of a temperature sensitive dye and a reference dye has to be found, that is excitable with the same light source, i.e. the dyes have a similar absorption spectrum, but have different emission spectra. To avoid type 1 spectral conflicts, i.e. an overlap of the signals (Coppeta and Rogers 1998), the emission bands should be clearly separated with a sufficiently large gap. At the same time the dependency of the signal ratio to temperature should be high in the desired temperature range in order to resolve small temperature changes. Additionally, both dyes have to be incorporated together in one particle with a concentration ratio that stays constant for all particles. Furthermore, the particle's luminescent signal has to be as high as possible, since the obtainable accuracy is directly related to the signal to noise ratio, as was shown in the previous chapter.

Vogt and Stephan (2012) used microcapsules as particles, which consisted of a solid polymer shell and a liquid core containing a mixture of the temperature sensitive dye Pyrromethene 597-8C9 and the reference dye Pyrromethene 567. They were able to achieve a large SNR of approximately 75, but the temperature sensitivity of the signal ratio was only 0.5% K^{-1}. However, this concept seems suitable, but the production of the particles was stopped by the manufacturer. To the authors knowledge no comparable microcapsules with a core consisting of a liquid solution of fluorescent dyes are commercially available at the moment.

An alternative possibility is the use of solid particles, that are doped with fluorescent dyes. These kind of particles are readily available and have been widely used in μ-PIV or μ-PTV measurements. They usually consist of a fluorescing dye (e.g. Rhodamine B) that is incorporated into a polymer matrix such as polystyrene (PS) or polymethylmethacrylat (PMMA). However, when incorporating a fluorescent dye in a solid matrix, its properties such as its temperature dependency may be severely altered. One example is Rhodamine B, which has a high temperature sensitivity of -1.5% K^{-1} when dissolved in water (Coppeta and Rogers 1998), which is reduced to only -0.12% K^{-1} for Rhodamine B doped PS-particles (Massing *et al* 2014). This sensitivity is too small to achieve the required temperature resolution. This effect can be explained by the fact that the dye molecules are immobilized inside the solid polymer matrix. In solution, the mobility of the dye molecules is increased, when the temperature is raised. This increases the probability of molecular collisions and as a consequence the probability of non-radiative de-excitation is increased as well, which reduces the luminescent intensity (Valeur and Berberan-Santos 2012). However, when the dye molecules are incorporated inside a solid polymer matrix, they stay relatively immobile irrespective of the temperature. Thus, the temperature dependency is severely reduced. After all, the behavior is specific to the combination of dye and polymer and 'since how the polymer affects the photophysical processes in the paint is not well understood, it is basically a trial and error process to find an optimal combination of a luminophore and a polymer' (Liu (2004), p 58).

A luminescent dye which shows a high temperature dependency of its emission intensity in different polymer materials is EuTTA (Basu and Vasantharajan 2008). Basu and Venkatraman (2009) successfully fabricated a bi-luminophore temperature sensitive paint consisting of EuTTA and perylene in polystyrene. They found a high temperature dependency of this combination of up to -1.8% K^{-1} depending on the dye concentrations. A big advantage of this combination is, that the emission spectra of perylene ($\sim$420–550 nm) and EuTTA ($\sim$575–635 nm) are far apart and do not overlap. This makes it easy to filter the respective signals. Nevertheless, if the appropriated dyes show sensitivities to other environmental parameters, their applicability may be limited. Ruthenium diimine complexes, for example, are known to have a temperature sensitive emission intensity but are additionally affected by molecular oxygen (Basu and Venkatraman 2009). However, EuTTA

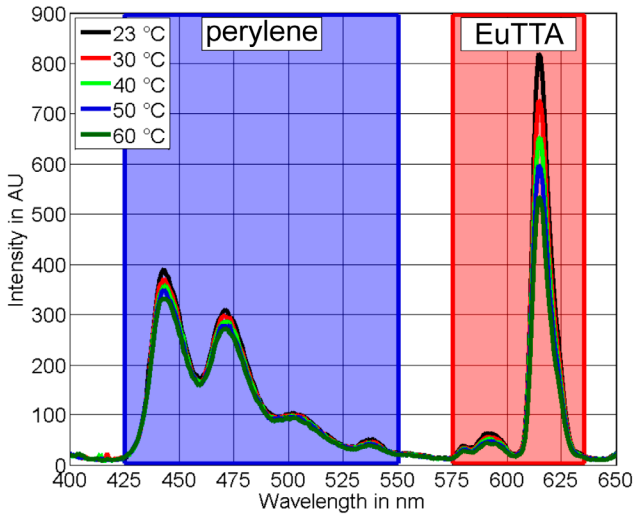

Figure 9. Emission spectrum of EuTTA/perylene particles at different temperatures.

and perylene did not experience luminescence quenching due to oxygen after they were incorporated into oxygen impermeable binders such as polystyrene or PMMA. Furthermore, to the authors knowledge, other sensitivities of the luminescence intensity of either species to their chemical environment, such as pH value, have not been reported. Zhu *et al* (2013) synthesized pressure and temperature dual-responsive PS-particles using EuTTA as the temperature sensitive dye and Coumarin 6 as the reference dye. The authors found a large temperature dependency of EuTTA in the order of $-2\%\ \mathrm{K}^{-1}$.

In this study luminescent PMMA polymer particles doped with perylene as a reference dye and the dye EuTTA as the temperature monitor are characterized as potential temperature sensitive tracers. The particles were synthesized by Surflay Nanotec GmbH. They were prepared via typical suspension polymerization (Yuan *et al* 1991, Arshady 1992). The organic phase contains the monomer, the luminescent dyes, the cross linking agent and the initiator, while the aqueous phase consists of a water soluble stabilizer and surfactants which is exemplified by Rodrigo *et al* (2012). The dye concentration for perylene is at solubility limit in the organic phase and for EuTTA at 0.5% related to monomer mass. Suspension of the organic phase in the aqueous phase takes place in a three necked round-bottomed jacketed glass reactor by Ultra-Turrax stirring treatment at 10 000 rpm for 10 min. After this, the dispersed phase is mechanically stirred at 300 rpm for 24 h at 60–70 °C, till the dispersed micro droplets are completely hardened. Finally, several washing steps in water are conduced to purify the suspension from reactants, whereas centrifugation steps served to narrow the particle size distribution. The measured emission spectra of the particles for different temperatures after an excitation at 340 nm is shown in figure 9. As expected, the intensity of the EuTTA emission significantly decreases with increasing temperature, whereas the emission intensity of perylene stays comparatively constant. This results in a temperature dependency of the ratio of the dye's emission intensities of approximately $-1.2\%\ \mathrm{K}^{-1}$. Additionally, the emission spectra of the two dyes do not

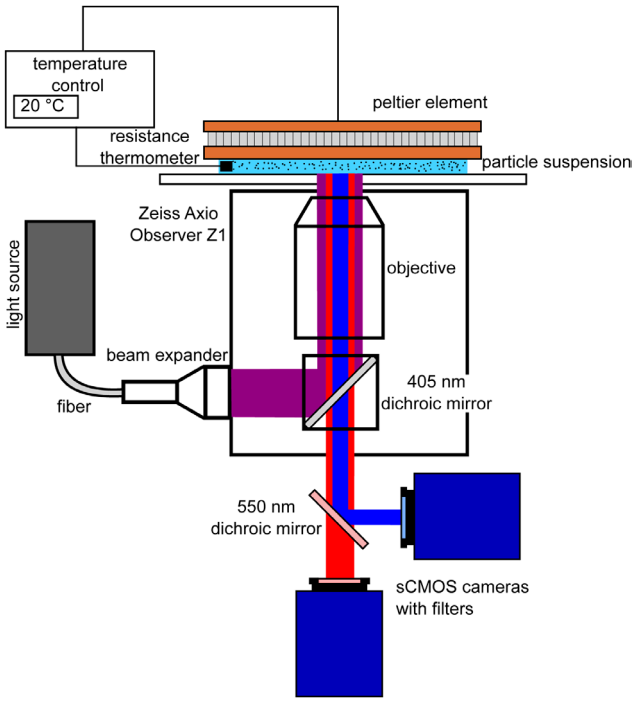

Figure 10. Schematic of the experimental set up.

overlap and can easily be separated without having cross-talk between the two cameras. Another important aspect is the temperature response time of the particles, which can be estimated by the following equation (Crowe *et al* 2011):

$$\tau_T = \frac{\rho_\mathrm{p} c_\mathrm{p} D_\mathrm{p}^2}{12 k_\mathrm{f}} \tag{1}$$

with ρ_p as the particle density, c_p as the specific heat capacity of the particle, D_p as the particle diameter and k_f as the thermal conductivity of the fluid. The thermal response time of the appropriated particles with a diameter of 10 μm in water is approximately 28 μs, which is sufficiently small for many microfluidic applications. However, the particles still have to be tested in an experimental setting, to evaluate their applicability as tracer particles for temperature sensing in microfluidics.

4.1. Experimental set-up

The experimental set-up used to characterize the applicability of EuTTA/Perylene doped PMMA—particles as temperature probes is shown in figure 10. For this task it is important to have a very well controlled experimental environment, which is quite challenging in microfluidics. To asses the measurement uncertainty associated with the particles, the temperature in their surrounding has to be known. Here, a droplet of an aqueous suspension of the particles was placed between a microscope slide and a peltier element and the temperature in the droplet was monitored with a Pt100 resistance thermometer (see figure 10). Thus, the temperature in the droplet could be set with a temperature control (CoolTronic TC282-RS232) within an accuracy of ± 0.1 K. To reduce background reflections the originally white peltier element

was painted black. The droplet was observed with a Zeiss Axio Observer Z1 microscope. To assess the influence of different magnifications the microscope was first equipped with a Zeiss LD Plan-Neofluar objective with a magnification of $M = 20$ and for comparison with a Zeiss EC Plan-Neofluar objective with a magnification of $M = 10$. Furthermore, different illumination strategies were tested. Initially, the luminescence of the particles was excited by a pulsed frequency tripled Nd:YAG laser with a wavelength of 355 nm (Innolas Spitlight 400). This means that the particles are exposed to a relatively strong excitation energy of 12 mJ, which is close to the damage threshold of the microscope, over a very short time of 5 ns (pulse width of the laser). However, the energy was not large enough to saturate the luminescence of either dye. Therefore, it can be expected that the laser illumination has no influence on the temperature response of the particles (Chaze *et al* 2016). The second light source that was used, was a UV-LED light with a peak emission wavelength of 365 nm and a maximum output power of 7 W (Luminus CBM-120-UV C31). The LED can be operated in pulsed mode, with the pulse width set equal to the camera's exposure time. Thus, the particles could be excited with low energy over a relatively long time (in the order of μs to ms).

The excitation light was guided through an optical fiber into a beam expander, which was connected to the microscope (see figure 10). A 405 nm dichroic mirror (Edmund Optics) reflected the illumination light onto the particle sample. The luminescent emission of the particles was then collected with the microscope objective and passed through the 405 nm dichroic mirror, which filtered a large portion of the laser and LED reflections. At the microscope camera outlet a 550 nm dichroic mirror (Edmund Optics) was placed to separate the temperature and reference signal (see figure 10). The signal of each dye was imaged separately with a 16 bit sCMOS camera (LaVision Imager sCMOS) with a CMOS-chip that consisted of 2160×2560 pixel. To remove the remaining laser reflections the reference camera was equipped with a 447 nm bandpass filter with a bandwidth of 60 nm and the temperature camera was equipped with a 625 nm bandpass filter with a bandwidth of 50 nm (both Edmund Optics). To match the reference and the temperature image, both cameras were connected to a set of microstages, which allowed for a precise control of the field of view of each camera.

The investigated temperature ranged from 20 °C to 60 °C with temperature steps of 5 °C. In order to examine the influence of the signal to noise ratio on the measurement uncertainty, imaging at each temperature step was done for different camera exposure times ($\tau_{exp} = 50$ μs, 100 μs, 250 μs, 500 μs, 1000 μs, 2500 μs, 5000 μs). Since the luminescent lifetime of the EuTTA-dye at room temperature is approximately 500 μs (Basu and Vasantharajan 2008) the temperature signal intensity depends on the camera exposure time in the investigated range, even when a short laser pulse was used as the excitation source. For the LED illumination the pulse width was set equal to the camera exposure time. Therefore, the illumination intensity and the SNR in both cameras depended on τ_{exp}.

To image particles at the different temperatures the following sequence was used. At the starting temperature 10 consecutive images were captured for each exposure time. Then, the droplet temperature was raised to the next temperature step and the imaged region was shifted to a different position in the droplet by moving the software controlled microscope stage 1500 μm in x-direction. Again 10 consecutive images were taken at the different exposure times. The procedure was repeated for each investigated temperature, which resulted in new particles at each temperature step. This rather complicated process was chosen to avoid the influence of photo bleaching on the intensity ratio, which is quite strong for these particles (approx. 3% decrease of the intensity ratio within the first 10 images, see figure 11). It is consistent with an experimental setting, where the temperature distribution in a microchannel with a continuous flow is measured. The cameras' frame rates can be adapted in such a way, that each image contains new particles. However, when time resolved measurements are necessary, the ratio has to be corrected for the effect of photo bleaching. Additionally, this process has the advantage, that the particle images at each temperature are uncorrelated, which gives a better statistic. Nevertheless, in each camera image only approximately 250 individual particle images were present, due to a relatively low seeding concentration. To obtain statistically stable results, the described sequence was repeated 3 times with different starting locations, which was the maximum number of tests that could be finished before the droplet was evaporated. This resulted in a number of approximately 750 individual particle images for each temperature.

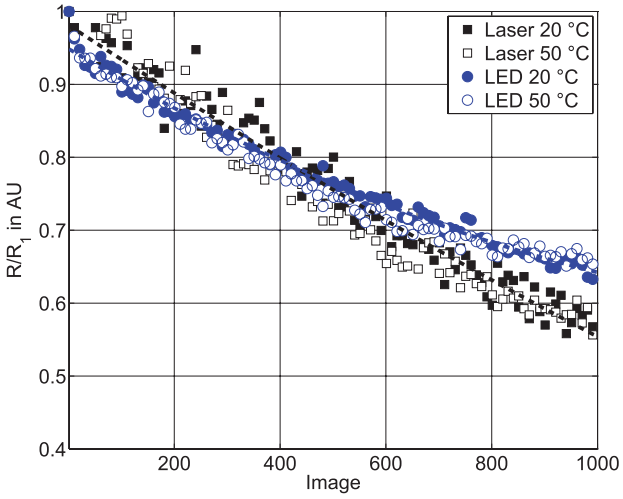

Figure 11. Effect of photobleaching on the intensity ratio of EuTTA/perylene particles within 1000 recorded images for laser and LED illumination at $T = 20$ °C and $T = 50$ °C.

4.2. Experimental results

Figure 12 shows the spatial distribution of the intensity ratio at a constant temperature of $T = 20$ °C, when a magnification of $M = 20$ and LED illumination was used. The intensity ratio exhibits a dependency on the particle image position in the X and Y plane, which corresponds to a second order polynomial fit as depicted in figure 12. Similar results were found for a magnification of $M = 10$ and for laser illumination at all

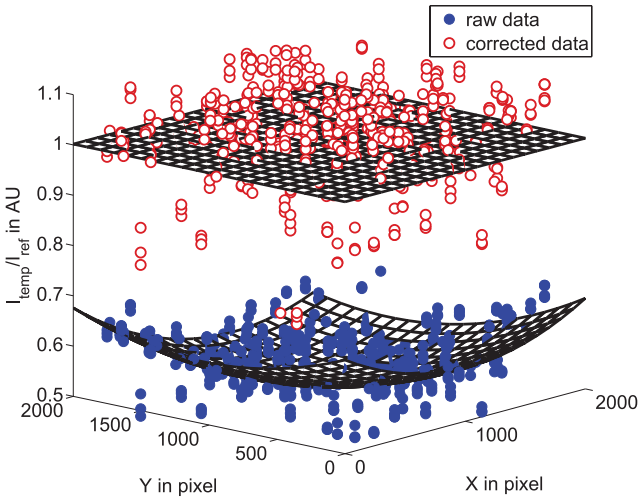

Figure 12. Spatial dependency of the raw intensity ratio and intensity ratio corrected for the X and Y position ($T = 20$ °C, $M = 20$, LED illumination).

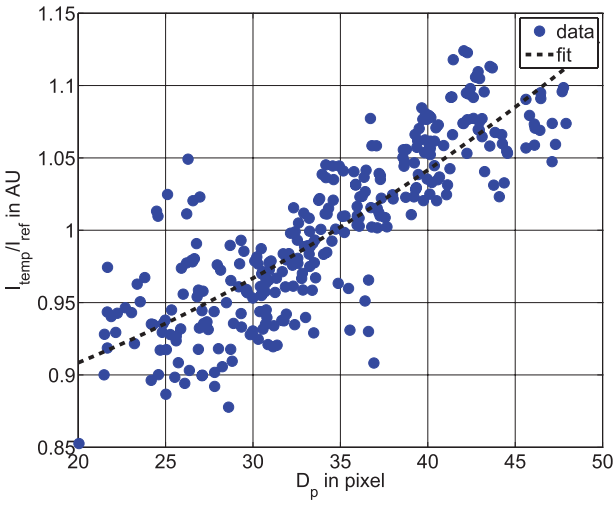

Figure 13. Dependency of the intensity ratio on the particle image diameter D_p ($T = 20$ °C, $M = 20$, LED illumination).

temperatures. At the first sight this seems unusual, since the reference dye should correct for spatial variations in the illumination intensity. However, this spatial variance is probably caused by imperfections in the optical lenses and filters in front of the cameras. Therefore, it is unrelated to the measured quantity and can be corrected by an appropriate calibration, prior to the experiment. Nevertheless, close to the borders of the field of view the X and Y dependency becomes quite strong when the camera's entire CMOS-chip is considered, which causes large measurement errors. To avoid this problem, only an area of 1900×2000 pixel is used, which is still more than enough to image the entire width of a 500 μm wide microchannel with a magnification of $M = 20$.

However, even after the ratio is corrected for the particle image position, the scatter in the intensity ratios in figure 12 is quite strong. This can be explained by the large variation of the particles' diameters (3 μm–10 μm). Labergue *et al* (2010) have shown, that when two-color LIF is used to measure the temperature of μm size droplets, the intensity ratio depends on the droplet size. This is caused by the fact that part of the fluorescent emission is re-absorbed by the fluorescent dye, due to an overlap in the emission and absorption spectrum. When the droplet size increases, the optical path length inside the droplet increases as well and the probability of re-absorption grows. For the dyes used in this investigation, only the spectra of the reference dye overlap. Therefore, it can be expected that the intensity ratio I_{temp}/I_{ref} increases with increasing particle diameter, since more of the reference emission is re-absorbed. Fortunately, in contrast to most macrofluidic applications, the particle image diameter in microfluidics is not diffraction limited, due to the large magnifications used. This means that the particle image diameter is a function of the physical particle diameter. Figure 13 shows the intensity ratio as a function of the particle image size. As expected, the intensity ratio increases with increasing particle image diameter. This has to be considered and corrected for during the experiment in order to obtain more accurate results for the temperature estimation. However, in most macrofluidic experiments where the particle image size is diffraction limited, mono disperse particles have to be used to avoid this effect and to obtain an accurate temperature estimation.

The uncertainty in estimating the temperature was determined in the following way. At each investigated droplet temperature, the intensity ratio of the individual particles' temperature and reference signals was computed and corrected for the particles' X and Y positions and particle image diameters. Then, similar to a temperature calibration, the mean value of all single particle image intensity ratios at each temperature step was calculated and the gradient of the mean ratios over the known droplet temperature was approximated with a second order polynomial fit. The temperature dependency of the intensity ratio was approximately -1.2% K^{-1}. Finally the fit was applied to the intensity ratios of the individual particle images, to give a temperature estimation for each recorded particle at the different droplet temperatures. In figure 14 the temperature that was estimated from the particle image intensity ratios for the different investigated magnifications and illumination techniques is plotted against the measured droplet temperature. The error-bars correspond to one standard deviation over all estimated temperature values. It can clearly be seen, that the mean estimated temperature is very close to the droplet temperature. When LED illumination is used, the absolute deviation of the mean estimated temperature from the prescribed droplet temperature ($\Delta T_{abs} = \langle |\overline{T_{est}} - T_{drop}| \rangle$) is only 0.2 K for a magnification of $M = 20$ and 0.3 K for $M = 10$. In the case of laser illumination the mean estimated temperature deviates from the droplet temperature by 0.5 K for both magnifications used. The mean standard deviations over the entire measured temperature range are ± 2.2 K for $M = 20$ and LED illumination, ± 2.6 K for $M = 10$ and LED illumination and ± 2.5 K for both magnifications and laser illumination. This corresponds to a 95% confidence interval of ± 4.4 K, ± 5.2 K and ± 5 K, respectively. The experiments were repeated for multiple droplets at different days with similar results. Furthermore, the error-bars in

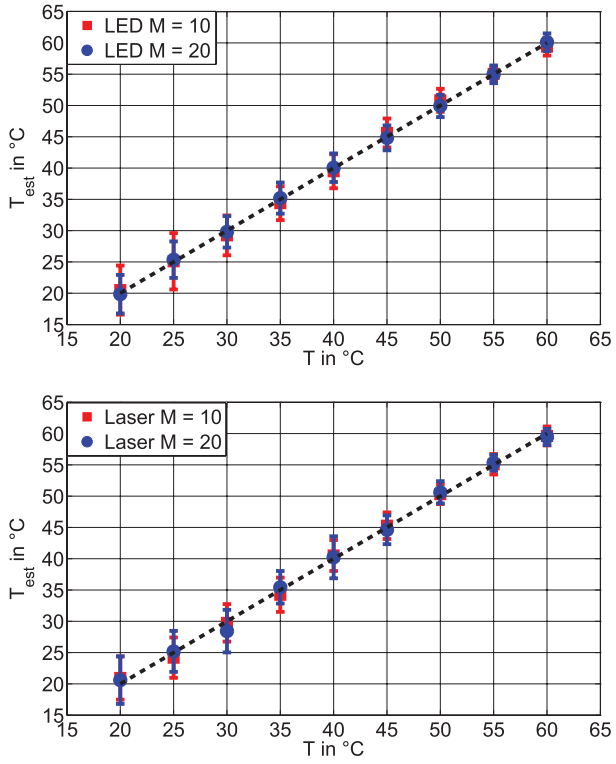

Figure 14. Estimated temperature plotted against prescribed droplet temperature for LED (top) and laser (bottom) illumination at different magnifications ($\tau_{exp} = 500$ μs).

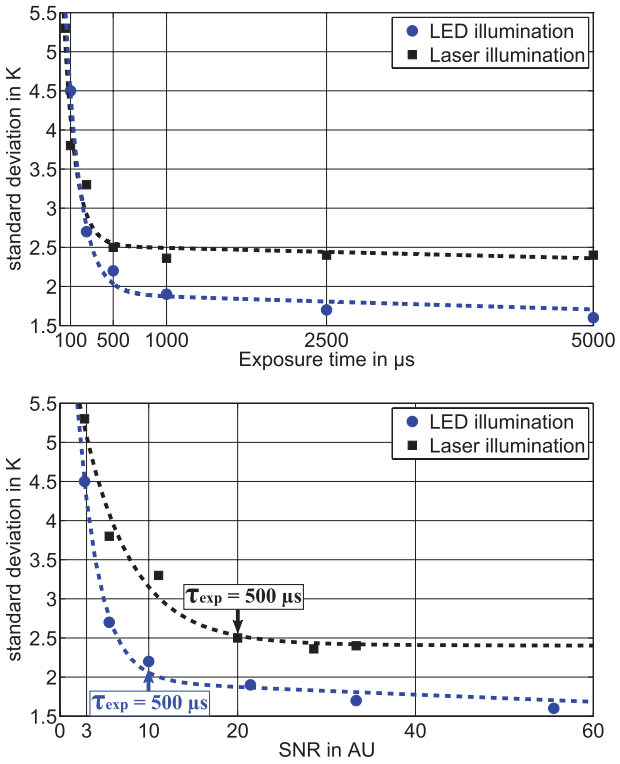

Figure 15. Standard deviation plotted against exposure time (top) and signal to noise ratio (bottom) for LED and laser illumination at a magnification of $M = 20$.

figure 14 are relatively constant over the entire measurement range, even though the temperature signal is significantly decreased at 60 °C. However, the signal is still high enough to allow for an accurate temperature estimation. Additionally, the temperature sensitivity of the EuTTA-dye shows no significant reduction at higher temperatures. Therefore, the measurement range can probably be extended further, without a significant increase in measurement uncertainty. This was not done in these experiments though, since the black paint used to reduce background reflections started to separate from the peltier element at temperatures above 60 °C.

The results in figure 14 were obtained whith a camera exposure time of 500 μs, which is the luminescent lifetime of the EuTTA-dye, i.e. the temperature camera records luminescent emission over the entire exposure time. This exposure time is low enough for the flow velocities in many microfluidic applications, but can cause streaking of the particle images in the temperature camera for high flow velocities. For the velocity estimation the reference image can simply be used, since perylene has a low fluorescent lifetime in the order of a few μs. For the temperature measurement, however, streaking in the temperature image will cause problems in the calculation of the intensity ratio. In order to avoid streaking, the camera exposure time has to be reduced, causing a reduction in signal intensity. Therefore, the signal to noise ratio is decreased, which increases the measurement uncertainty as was shown in section 3. Figure 15 shows the mean standard deviation over the measured temperature range as a function of the appropriated exposure time and signal to noise ratio. As was predicted from the synthetic images in section 3 the measurement uncertainty is a second order exponential function of the signal to noise ratio and hence of the exposure time for both LED and laser illumination. For LED illumination, the measurement uncertainty increases rapidly for signal to noise ratios below 10, but decreases quite slowly for larger signal to noise ratios. However, the measurement uncertainty for lower SNRs increases faster than what was found in section 3. This is caused by the effect, that not only the intensity, but also the lifetime of the EuTTA-dye decreases with increasing temperature. When a camera exposure time of less than 500 μs is used, only a smaller part of the luminescent emission is integrated on the camera chip. This means that for smaller exposure times the decrease in the recorded EuTTA signal intensity with increasing temperature is reduced. For a given standard deviation, a smaller signal over temperature gradient leads to higher measurement uncertainties. Since the signal to noise ratios smaller than 10 are associated with exposure times of less than 500 μs, this effect additionally adds to the increase in measurement uncertainty. Consequently, the accuracy of the temperature estimation decreases faster than what was predicted on the basis of the synthetic images, where only the influence of smaller SNRs was considered. However, for LED illumination an exposure time of 250 μs leads to a standard deviation of ± 2.7 K, which is still tolerable for temperature estimation in many cases. Choosing exposure times below 250 μs, though, leads to a much higher measurement uncertainty and going below 100 μs additionally introduces the problem, that the temperature signal at 60 °C is almost vanished. This

makes it nearly impossible to identify particle images, thus, reducing the applicable measurement range.

In case of laser illumination, overall the SNRs that can be reached at exposure times below 1000 μs are higher compared to the LED illumination, due to the higher excitation energy. For larger exposure times, the illumination energy of the LED surpasses the laser illumination, because the LED excitation energy increases with exposure time (the pulse width is set equal to the exposure time), whereas the laser energy stays constant (constant pulse width). However, in case of laser illumination the measurement uncertainty already starts significantly increasing earlier than in the LED experiments, at SNRs below 20. This increase in uncertainty is mainly caused by the fact, that the measured points with a SNR below 20 are associated with an exposure time of less than 500 μs, i.e. the temperature dependency of the intensity ratio is lowered. Nevertheless, at low exposure times of less than 100 μs the laser illumination gives a smaller standard deviation ($\pm$3.8 K for $\tau_{exp} = 100$ μs), due to the higher signal intensity. Additionally, even at 60 °C the temperature signal is still high enough to easily identify particle images at lower exposure times. Therefore, in contrast to the LED illumination, the measurement range is not limited. However, the standard deviation when laser illumination is used is slightly higher than the standard deviation when LED illumination is used for an exposure time of 500 μs, even though the SNR is 2 times as high. As can be seen in figure 15, though, the signal to noise ratio is already in the region, where an increase in signal intensity only slightly reduces the standard deviation. Furthermore, when the standard deviation for this point is compared to the standard deviation at the same SNR with LED illumination, it is approximately 0.8 K larger. The reason for this is probably the relatively low pulse-to-pulse stability of the laser, compared to the very stable LED. Even though the reference dye should correct for this, the rationing is not perfect and a slight temporal fluctuation is still present. This causes the increase in the standard deviation and also in ΔT_{abs} from 0.2 K to 0.5 K. It can be stated, that laser illumination should be used when the flow velocities demand for exposure times below 250 μs. For higher exposure times LED illumination leads to more accurate temperature estimations.

5. Conclusion

Presented herein, a luminescent particle based method for simultaneous non-intrusive temperature and velocity measurements was introduced. To determine the temperature, the ratio of the reference and the temperature signal intensities of individual dual-color luminescent particles is analyzed. The technique is particularly suited for microfluidic applications, because it is not biased by strong in-plane or out-of-plane gradients, even if volume illumination is used. Different methods of calculating the intensity ratio of individual particle images were evaluated on the basis of synthetic particle images. The results show, that approximating the noisy particle images with a 2D Gaussian and using the mean of the fitted intensity values for rationing leads to the lowest measurement uncertainty. Furthermore, the results show a strong dependency of the measurement accuracy on the particle image diameter and on the SNR, especially for SNRs < 10. Therefore, the luminescent particle signal has to be as high as possible to allow for reliable temperature estimations.

Based on these findings, dual-color luminescent polymer tracers doped with perylene and EuTTA (synthesized by the Surflay Nanotec GmbH) were investigated for their applicability as temperature probes in microfluidic experiments. The experimental results show an absolute deviation of the mean estimated temperature from the prescribed temperature of $\Delta T_{abs} = 0.2$ K and an uncertainty of $\pm$4.4 K for a 95% confidence interval, when LED illumination and a magnification of $M = 20$ is used. When a laser is used as the light source, the uncertainty increases to $\Delta T_{abs} = 0.5$ K and an uncertainty of $\pm$5.0 K for a 95% confidence interval, which was attributed to the relatively large pulse-to-pulse fluctuations in the laser energy. Even though, using an intensity ratio mostly corrects for these fluctuations, there are still small variations in the ratio present, which lead to a higher measurement uncertainty. Therefore, it can be concluded that the stability of the light source is important for reliable measurements.

However, it was shown that the measurement technique and the appropriated particles are a valid tool for non-intrusive temperature field measurements in microfluidics in a temperature range between 20 °C and 60 °C. This range surpasses the temperature bandwidth of currently available TLC materials and can probably be increased further without loss of measurement accuracy.

LED illumination should be used, when the flow velocity allows for exposure times of at least 250 μs. When lower exposure times are necessary, laser illumination leads to a smaller measurement uncertainty, due to larger signal to noise ratios. Additionally, it was shown that the intensity ratio exhibits a strong dependency on the particle diameter, due to re-absorption of the reference emission. Even though this can be corrected for in microfluidics, synthesizing particles with a narrower diameter distribution than the current 3–10 μm would be desirable, to further reduce the measurement uncertainty. If monodisperse particles are used, they can even become applicable for measurements on the macroscopic scale.

Acknowledgments

Financial support from the German Research Foundation (DFG), under the framework of the Emmy-Noether grant 'Kontrollierte elektrochemische Energieumwandlung durch oberflächennahe Strömungsbeeinflussung' (CI 185/3) and from the 'Arbeitsgemeinschaft industrieller Forschungsvereinigungen' (AiF) under the grant 'Schnellstart: Entwicklung eines Verfahrens zum gezielten Vorheizen einer Direkt-Methanol-Brennstoffzelle mit minimalem Energieaufwand' (18941 N), is gratefully appreciated.

The authors would like to thank Dana Dabiri and Gamal Khalil for the fruitful discussions and helpful advice.

References

Abram C, Fond B and Beyrau F 2015 High-precision flow temperature imaging using ZnO thermographic phosphor tracer particles *Opt. Express* **23** 19453–68

Adrian R J 1991 Particle-imaging techniques for experimental fluid mechanics *Annu. Rev. Fluid Mech.* **23** 261–304

Aldén M, Omrane A, Richter M and Särner G 2011 Thermographic phosphors for thermometry: a survey of combustion applications *Prog. Energy Combust. Sci.* **37** 422–61

Arshady R 1992 Suspension, emulsion, and dispersion polymerization: a methodological survey *Colloid Polym. Sci.* **270** 717–32

Basu B J and Vasantharajan N 2008 Temperature dependence of the luminescence lifetime of a europium complex immobilized in different polymer matrices *J. Lumin.* **128** 1701–8

Basu B J and Venkatraman S 2009 Fabrication of a bi-luminophore temperature sensitive coating by embedding europium thenoyltrifluoroacetonate (EuTTA) and perylene in polystyrene *J. Fluorescence* **19** 479–85

Chaze W, Caballina O, Castanet G and Lemoine F 2016 The saturation of the fluorescence and its consequences for laser-induced fluorescence thermometry in liquid flows *Exp. Fluids* **57** 1–18

Cierpka C and Kähler C J 2012 Particle imaging techniques for volumetric three-component (3D3C) velocity measurements in microfluidics *J. Vis.* **15** 1–31

Cierpka C, Lütke B and Kähler C J 2013 Higher order multi-frame particle tracking velocimetry *Exp. Fluids* **54** 1533

Cierpka C, Segura R, Hain R and Kähler C J 2010 A simple single camera 3C3D velocity measurement technique without errors due to depth of correlation and spatial averaging for microfluidics *Meas. Sci. Technol.* **21** 045401

Coppeta J and Rogers C 1998 Dual emission laser induced fluorescence for direct planar scalar behavior measurements *Exp. Fluids* **25** 1–15

Crimaldi J 2008 Planar laser induced fluorescence in aqueous flows *Exp. Fluids* **44** 851–63

Crowe C T, Schwarzkopf J D, Sommerfeld M and Tsuji Y 2011 *Multiphase Flows With Droplets and Particles* (Boca Raton, FL: CRC Press)

Dabiri D 2009 Digital particle image thermometry/velocimetry: a review *Exp. Fluids* **46** 191–241

Faghri A and Guo Z 2005 Challenges and opportunities of thermal management issues related to fuel cell technology and modeling *Int. J. Heat Mass Transfer* **48** 3891–920

Fond B, Abram C and Beyrau F 2015 Characterisation of the luminescence properties of BAM: Eu^2+ particles as a tracer for thermographic particle image velocimetry *Appl. Phys.* B **121** 495–509

Fond B, Abram C, Heyes A L, Kempf A M and Beyrau F 2012 Simultaneous temperature, mixture fraction and velocity imaging in turbulent flows using thermographic phosphor tracer particles *Opt. Express* **20** 22118–33

Hiller W *et al* 1993 Onset of natural convection in a cube *Int. J. Heat Mass Transfer* **36** 3251–63

Kähler C J 2004 The significance of coherent flow structures for the turbulent mixing in wall-bounded flows *PhD Thesis* Georg-August-Universität Göttingen

Kähler C J, Astarita T, Vlachos P P, Sakakibara J, Hain R, Discetti S, Foy R and Cierpka C 2016 Main results of the 4th international PIV challenge *Exp. Fluids* **57** 1–71

Kähler C J, Scharnowski S and Cierpka C 2012 On the uncertainty of digital PIV and PTV near walls *Exp. Fluids* **52** 1641–56

Kim M and Yoda M 2010 Dual-tracer fluorescence thermometry measurements in a heated channel *Exp. Fluids* **49** 257–66

Kim M M, Giry A, Mastiani M, Rodrigues G O, Reis A and Mandin P 2015 Microscale thermometry: a review *Microelectron. Eng.* **148** 129–42

Kimura I, Takamori T, Yamauchi H, Ozawa M, Takenaka N and Sakaguchi T 1988 Simultaneous measurement of flow and temperature fields based on color image information *Nagare No Kashika* **8** 185–8

Labergue A, Deprédurand V, Delconte A, Castanet G and Lemoine F 2010 New insight into two-color LIF thermometry applied to temperature measurements of droplets *Exp. Fluids* **49** 547–56

Liu T 2004 *Pressure-and Temperature-Sensitive Paints* (New York: Wiley)

Massing J, Irwansyah R, Kähler C and Cierpka C 2014 Optische temperaturmessung in der mikrofluidik mittels temperatursensitiver fluoreszenter partikel *Fachtagung Lasermethoden in der Strömungsmesstechnik (Karlsruhe, September 2014)*

Meinhart C D and Wereley S T 2003 The theory of diffraction-limited resolution in microparticle image velocimetry *Meas. Sci. Technol.* **14** 1047–53

Natrajan V K and Christensen K T 2009 Two-color laser-induced fluorescent thermometry for microfluidic systems *Meas. Sci. Technol.* **20** 015401

Rodrigo R, Toro C A and Cuellar J 2012 Influence of the geometric factors of the experimental device used in suspension polymerization on the properties of poly (styrene-co-divinylbenzene) microparticles *J. Appl. Polym. Sci.* **124** 1431–46

Sakakibara J and Adrian R J 1999 Whole field measurement of temperature in water using two-color laser induced fluorescence *Exp. Fluids* **26** 7–15

Schiepel D, Schmeling D and Wagner C 2016 Simultaneous velocity and temperature measurements in turbulent Rayleigh–Bénard convection based on combined Tomo-PIV and PIT *Proc. of the 18th Int. Symp. on Application of Laser and Imaging Techniques to Fluid Mechanics (Lisbon, July 2016)*

Segura R 2014 Thermo-liquid crystal (TLC) thermography and astigmatism particle tracking velocimetry (APTV) for the simultaneous time-resolved 3D measurements of microscopic temperature and velocity flow fields *PhD Thesis* Bundeswehr University Munich

Segura R, Cierpka C, Rossi M, Joseph S, Bunjes H and Kähler C J 2013 Non-encapsulated thermo-liquid crystals for digital particle tracking thermography/velocimetry in microfluidics *Microfluid. Nanofluid.* **14** 445–56

Segura R, Rossi M, Cierpka C and Kähler C J 2015 Simultaneous three-dimensional temperature and velocity field measurements using astigmatic imaging of non-encapsulated thermo-liquid crystal (TLC) particles *Lab Chip* **15** 660–3

Shafii M, Lum C and Koochesfahani M 2010 *In situ* LIF temperature measurements in aqueous ammonium chloride solution during uni-directional solidification *Exp. Fluids* **48** 651–62

Valeur B and Berberan-Santos M N 2012 *Molecular Fluorescence: Principles and Applications* (New York: Wiley)

Vogt J and Stephan P 2012 Using microencapsulated fluorescent dyes for simultaneous measurement of temperature and velocity fields *Meas. Sci. Technol.* **23** 105–306

Yoshida H 2005 The wide variety of possible applications of micro-thermofluid control *Microfluid. Nanofluid.* **1** 289–300

Yuan H, Kalfas G and Ray W 1991 Suspension polymerization *J. Macromol. Sci. C: Polym. Rev.* **31** 215–99

Zhu C, Deng R, Zeng J, Khalil G E, Dabiri D, Gu Z and Xia Y 2013 Synthesis and characterization of pressure and temperature dual-responsive polystyrene microbeads *Part. Part. Syst. Charact.* **30** 542–8